PCCP

Spectral Analysis and Kinetic Modeling of Radioluminescence in Air and Nitrogen

Journal:	*Physical Chemistry Chemical Physics*
Manuscript ID	CP-ART-12-2023-006198.R1
Article Type:	Paper
Date Submitted by the Author:	18-Mar-2024
Complete List of Authors:	Jans, Elijah; Sandia National Laboratories, Casey, Ternan; Sandia National Laboratories Marshall, Garrett; Sandia National Laboratories Murzyn, Christopher; Sandia National Laboratories Harilal, Sivanandan; Pacific Northwest National Laboratory, National Security McDonald, Benjamin; Pacific Northwest National Laboratory, National Security Harrison, Richard; Sandia National Laboratories

Spectral Analysis and Kinetic Modeling of Radioluminescence in Air and Nitrogen

E.R. Jans[a,*], T. Casey[b], G. Marshall[a], C.M. Murzyn[a], S.S. Harilal[c], B.S. McDonald[c], R.K. Harrison[a]

[a] *Sandia National Laboratories, 1515 Eubank Blvd SE, Albuquerque, NM*
[b] *Sandia National Laboratories, P.O. Box 969, Livermore, CA*
[c] *Pacific Northwest National Laboratory, 902 Battelle Blvd, Richland, WA*

Abstract

In this article we present a quantitative analysis of the second positive system of molecular nitrogen and first negative system of molecular nitrogen cation excited in the presence of ionizing radiation. Optical emission spectra of atmospheric air and nitrogen surrounding ^{210}Po sources were measured from 250 - 400 nm. Multi-Boltzmann and non-Boltzmann vibrational distribution spectral models were used to determine the vibrational temperature and vibrational distribution function of the emitting $N_2(C^3\Pi_u)$ and $N_2^+(B^2\Sigma_u^+)$ states.A zero-dimensional kinetic model, based on the electron energy distribution function (EEDF) and a steady-state excitation and de-excitation of $N_2(X^1\Sigma_g^+)$, $N_2^+(B^2\Sigma_u^+)$, $N_2^+(X^2\Sigma_g^+)$, N_4^+, O_2^+, and $N_2(C^3\Pi_u, v)$, was developed for the prediction of the relative spectral intensity of both the $N_2^+(B^2\Sigma_u^+ \rightarrow X^2\Sigma_g^+)$ emission band and the vibrational bands of $N_2(C^3\Pi_u \rightarrow B^3\Pi_g)$ for comparison with the experimental data.

Keywords: alpha radiation, spectral modeling, vibration distribution function, kinetic modeling

1. Introduction

Optical imaging approaches for detecting ionizing radiation have seen increased interest for identification of radioactive materials and contaminated areas (1; 2; 3; 4; 5; 6). The technique enables localization of ionizing radiation from low-dose regions by leveraging longer attenuation lengths of optical photons in air compared to ionizing photons/particle emissions. Optical photon production begins with a radioactive decay which ionizes constituent molecules of air. Secondary electrons from this event continue to interact with the environment by exciting molecules to higher electronic states. Optical photons are then generated in a process known as radioluminescence as excited electronic, vibrational, and rotational states decay to lower energy levels. Nearly 99% of the radioluminescence caused by alpha particles is between 280-440 nm consisting primarily of the $N_2(C^3\Pi_u \rightarrow B^3\Pi_g)$ second positive system and $N_2^+(B^2\Sigma_u^+ \rightarrow X^2\Sigma_g^+)$ first negative system (7).

The radioluminescence spectrum generated by ionizing radiation excitation is similar to that of other forms of air plasmas (8; 9). However, comparison of the literature shows up to 2x disagreement for some of the major second positive band ratios (10). To study this discrepancy and inform deployable optical imaging techniques for targeted scenarios, a methodology to predict the fluorescence spectrum from a given radioactive source is desirable. Thompson, et al. developed a Geant4 model to study fluorescence from alpha, beta, and gamma sources (11). Their model differed from contemporary tools used to simulate cosmic beta radiation (12; 13; 14) which consisted of higher energy particles than those produced from radioactive sources. In the radioactive emission case, electron cascades are expected to be more sensitive to the initial particle (11). In their model, Thompson et al. saw good agreement between simulated fluorescence and measured absolute yield from the literature (2). Lalau and Ioan used a Monte Carlo method to determine optical emission ratios between alpha-excited air and Cherenkov photons in mixed alpha-beta environments (15). While effective, both models predicted fluorescence as Dirac functions limiting the ability to accurately predict spectral shapes to estimate response of deployed imaging equipment. However, while spectral modeling tools have been used to fit spectral emission for vibrational and rotational temperatures in electron beams (16) and air plasmas, (17; 18) no spectral analysis has been performed for radioluminescence generated by alpha particles.

This article summarizes the spectroscopic analysis and progress in forward modeling of radioluminescence generated in atmospheric air and nitrogen by alpha particles. High- and low-resolution emission spectra from 250-400 nm were taken from two different ^{210}Po sources. To analyze the emission spectra, a multi-Boltzmann spectral model for fitting rotational and vibrational temperatures of the measured $N_2(C^3\Pi_u \rightarrow B^3\Pi_g)$ second positive system and $N_2^+(B^2\Sigma_u^+ \rightarrow X^2\Sigma_g^+)$ first negative system was developed. Improvements to the spectral modeling with the inclusion of fitting a non-Boltzmann vibrational distribution function (VDF) to the emission spectra highlights the complexity of the radioluminescence of alpha particles. Finally, a simplified zero-dimensional kinetic model of radioluminescence in air and nitrogen is compared to the experimental data. Specifically, the comparison of the VDF of the $N_2(C^3\Pi_u)$ molecule and the relative population ratio of

*Corresponding Author
Email address: erjans@sandia.gov (E.R. Jans)

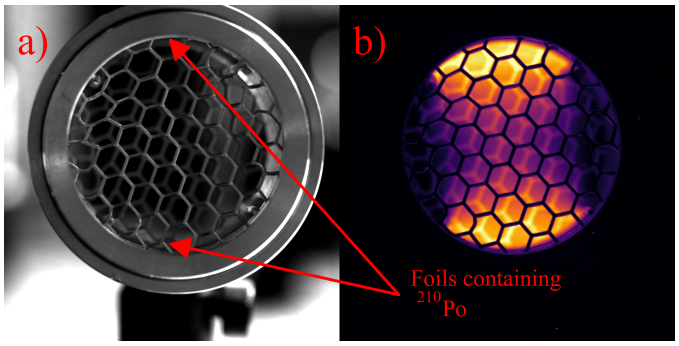

Figure 1: (a) Image of the aluminum housing containing the ^{210}Po samples. (b) A heat map from a 60-minute exposure taken with an Andor monochrome iKon camera and a 300-400 nm filter of the optical emission from the ^{210}Po samples.

$N_2(C^3\Pi_u)$ to $N_2^+(B^2\Sigma_u^+)$ is used to assess the overall predictive capability of the kinetic mechanism for forward modeling estimates.

2. Experimental Set-up

2.1. Sandia ^{210}Po Source and Experimental Set-up

The experimental set-up for acquiring optical emission has been discussed in detail elsewhere (10). Briefly, a P-2035 ^{210}Po source from NRD, LLC was used to measure ultraviolet (UV) ambient air emission from 250-400 nm at T = 293 K, p = 83 kPa and a relative humidity (RH) between 20-40%. An aluminum housing contained the two diametrically opposed ^{210}Po samples covered by thin gold foils. An image of the aluminum housing containing the ^{210}Po samples is shown in Fig. 1(a). A 60-minute exposure of the optical emission from the ^{210}Po samples was taken with an Andor monochrome iKon camera and a 300-400 nm filter shows the intensity distribution from the interaction of the alpha particles with air in Fig. 1(b). For the spectrally resolved emission measurements, the mesh was removed from the aluminum housing. To acquire the UV emission, an Andor Kymera 328i Czerny-Turner spectrometer with a 2400 grooves/mm grating blazed at 300 nm was used with a slit width of 25.4 µm. The ^{210}Po source was placed directly at the entrance of the slit of the spectrometer with a UV-enhanced aluminum mirror placed at the back of the source to increase the collection efficiency into the spectrometer. To acquire the spectra, an Andor iKon-M934-BU2 back-illuminated CCD camera was cooled to -90 °C and took nine-hour exposures of the ^{210}Po source over the course of over nine days. Over the nine days, the ^{210}Po source activity varied between 601–551 MBq (16.69–15.31 mCi for each individual source). To collect spectra from 250-450 nm, a series of binned images of 128 x 1024 (i.e. binned along intensity, not wavelength) were taken with a spectral range of ~14 nm and stitched together. Images were taken to remove intensity spikes from direct gamma-strikes on the camera chip.

Wavelength calibration for each 14 nm segment was done using Hg, Ne, Kr, or Ar emission lines between 237–436 nm. Calibration wavelengths were provided by the lamps' manufacturer (19). The spectral resolution of the system was determined from the average full-width at half-maximum (FWHM) of Hg emission lines for a resolution of 0.063 nm. A NIST-traceable OceanOptics DH3-Plus calibrated light source was used for a relative intensity correction for the entire spectrum. The majority of the emission collected from the ^{210}Po was from the N_2 second positive system along with the N_2^+ first negative system as shown in Fig. 2. Figure 2 has the different band progressions, $\Delta v = v' - v''$, for the second positive system (SPS) and first negative system (FNS) labeled for reference. The first negative system $N_2^+(B^2\Sigma_u^+, v = 0 \rightarrow X^2\Sigma_g^+, v = 0)$ shows up at the end of the $\Delta v = -3$ band progression at 391 nm. A number of other nitrogen electronic bands of low intensity were also measured such as the Gaydon-Herman bands (20).

2.2. PNNL ^{210}Po Source and Experimental Set-up

A similar ^{210}Po source (model P-2035) was used to induce air fluorescence at Pacific Northwest National Laboratory (PNNL) with an activity ~ 740 MBq (20 mCi) for each of the two alpha sources contained in the Al housing. The spectroscopic measurements were carried out by isolating the source in a vacuum chamber to allow for pressure variation from 14.6 to 101.3 kPa of ambient air (T = 22 °C and RH = 22%) and measurements in pure nitrogen. The chamber included a 76.2 mm square quartz port for light collection.

An optical system consisting of two plano-convex lenses was used for transporting the radioluminescence signals onto the slit of a 0.32 m grating spectrometer (Isoplane, Teledyne Inc.). Broad UV spectral measurements were collected using a 300 g/mm grating blazed at 300 nm and imaged on an iCCD camera (PiMAX4, Princeton Instruments), providing a spectral resolution of ~1.17 nm. The the relative intensity of the spectroscopic system was, likewise, corrected using a radiometrically calibrated light source (Ocean Optics DH-3 plus). The primary electronic emission bands measured in the PNNL source were again N_2 SPS along with the N_2^+ FNS. The radioluminescence from PNNL's set-up is shown in Fig. 2.

3. Spectral Modeling and Comparison

To facilitate analysis of the observed emission spectra induced by radioactive decay, a rework of the foundational mechanics in Sandia's SPEARS spectral modeling code (21) was performed. Common spectral modeling approaches use thermal equilibrium which assumes that the temperatures for the rotational, vibrational, and electronic Boltzmann distributions are all equal. A more precise spectral model allows for each quantum mode (i.e. rotational, vibrational, and electronic) to have an independent Boltzmann distribution as shown in Eq. 1:

$$\frac{n_i(T_r, T_v, T_e)}{n} = \frac{g_i exp\left(\frac{-e_r}{k_B T_r}\right) exp\left(\frac{-e_v}{k_B T_v}\right) exp\left(\frac{-e_e}{k_B T_e}\right)}{Z_r Z_v Z_e} \quad (1)$$

where k_B is the Boltzmann constant, g_i is state degeneracy, and Z_i is the partition function with $i = r, v$, and e equal to rotational, vibrational, and electronic modes. The state population, n_i, is for a specific rotational, vibrational, and electronic state

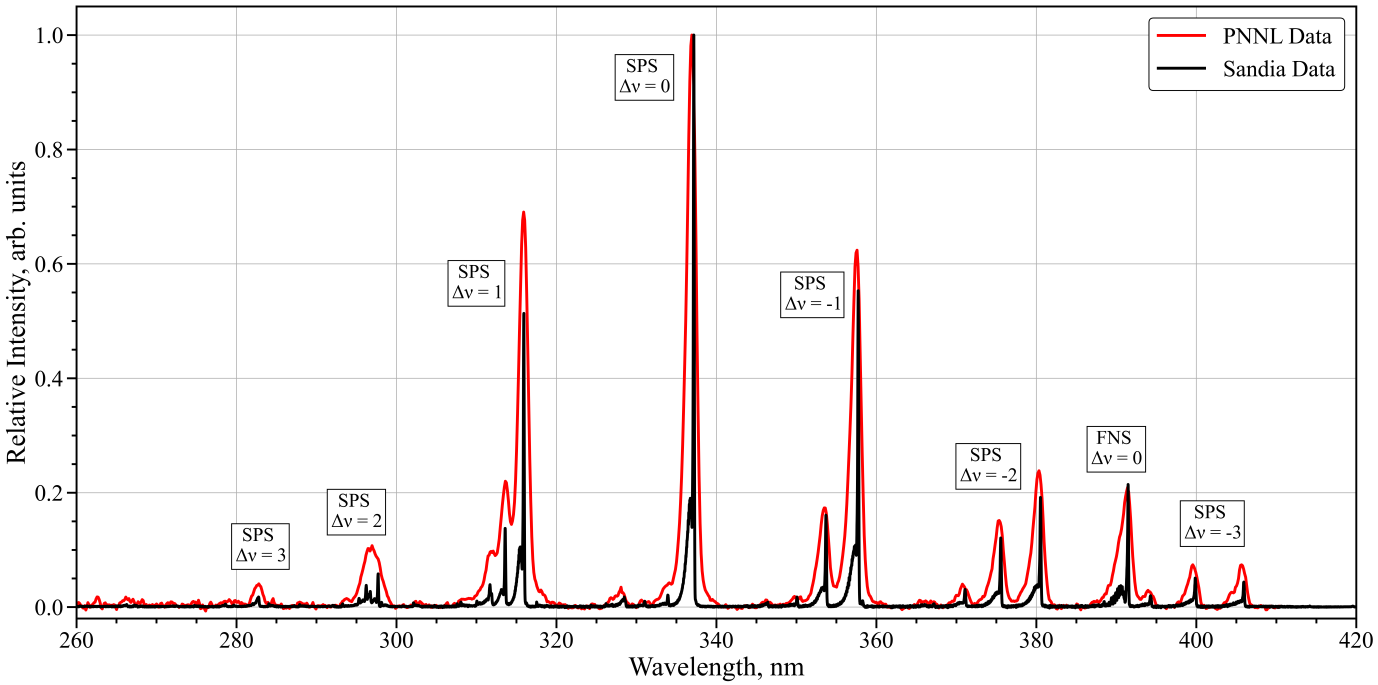

Figure 2: Comparison of radioluminescence spectra from (a) high resolution spectrum of the Sandia ^{210}Po source in ambient air at T = 293 K and p = 83 kPa and (b) low-resolution spectrum of the PNNL ^{210}Po source in ambient air at T = 293 K and p = 101.3 kPa.

which is defined by a rotational e_r, vibrational e_v, and electronic e_e energies. In this framework, emission spectra can be expressed by characteristic temperatures such as: rotational temperature T_r, vibrational temperature T_v, and electronic temperature T_e. Assuming the emitting slab of gas to be optically thin, re-absorption of emitted photons becomes negligible.

When the emission spectra are kinetically driven, such as in the presence of ionizing radiation, the resulting spectra may no longer follow Boltzmann statistics (22). Therefore, for proper analysis the spectral modeling must accommodate a non-Boltzmann VDF. To do so, the radiative cross-sections are organized in a $m \times v$ matrix where m is the number of frequency points and v is the number of vibrational states included in the VDF. The calculated radiative cross-sections include the rotational Boltzmann distribution functions from Eq. 1 while the vibrational Boltzmann distribution is removed. From there, a simple matrix multiplication is performed to generate an emission spectrum as illustrated in Eq. 2

$$\begin{bmatrix} I(\nu_1) \\ I(\nu_2) \\ \vdots \\ I(\nu_m) \end{bmatrix} = \begin{bmatrix} \sigma_1(\nu_1) & \sigma_2(\nu_1) & \cdots & \sigma_n(\nu_1) \\ \sigma_1(\nu_2) & \sigma_2(\nu_2) & \cdots & \sigma_n(\nu_2) \\ \vdots & \vdots & \ddots & \vdots \\ \sigma_1(\nu_m) & \sigma_2(\nu_m) & \cdots & \sigma_n(\nu_m) \end{bmatrix} \begin{bmatrix} \mathrm{v}_1 \\ \mathrm{v}_2 \\ \vdots \\ \mathrm{v}_n \end{bmatrix} \quad (2)$$

where $I(\nu_m)$ is the spectral emission intensity at frequency ν_m and $\sigma_n(\nu_m)$ is the optical radiative cross-section at frequency ν_m for the v_n vibrational state. The vibrational vector array of $[v_1, v_2, \ldots, v_n]$ is comprised of relative vibrational number densities from 0 to 1. The optical radiative cross-section ($\mathrm{W{\cdot}m^{-2}{\cdot}sr^{-1}{\cdot}Hz^{-1}}$) for a single transition in vibrational state n is defined as:

$$\sigma_n(\nu) = \frac{h\nu_{ul}}{4\pi} n_u A_{ul} g(\nu - \nu_0) l \quad (3)$$

where h is Planck's constant, ν_{ul} is the transition frequency, A_{ul} is the Einstein emission coefficient, $g(\nu - \nu_0)$ is the lineshape function, and l is the path length. The upper state number density, n_u, assumes a rotational Boltzmann distribution, $g_i exp\left(\frac{-e_r}{k_B T_r}\right)$, from Eq. 1 but has no vibrational Boltzmann distribution, $exp\left(\frac{-e_v}{k_B T_v}\right)$. Instead, the optical radiative cross-section is matrix multiplied by an arbitrary VDF to collapse the matrix into a single array containing the synthetic emission spectrum.

To fit the measured N_2 SPS spectra, the spectral linelist from Ref. (23) for N_2 SPS was used. The entire linelist was used with J_{max} = 150 for both states and v_{max} = 29 and 4 for the $B^3\Pi_g$ and $C^3\Pi_u$, respectively. The N_2^+ FNS experimental spectra was fit from data compiled from the LIFBASE software (24) with J_{max} = 84.5 for both states and v_{max} = 10 and 6 for the $X^2\Sigma_g^+$ and $B^2\Sigma_u^+$, respectively. A Nelder-Mead optimizer was used for fitting the multi-Boltzmann SPEARS model by minimizing the sum of squared residuals between the experimental data and modeled spectral radiance. The optimization simultaneously fit the rotational and vibrational temperatures and the instrument broadening. The instrument broadening from both spectrometers was assumed to be Gaussian. The fitted vibrational temperatures from Sandia and PNNL are given in Table 1 for air at p = 101, 83, and 15 kPa and for pure nitrogen. The average vibrational temperature of the $N_2(C)$ molecule is close to ~3800 K while for pure nitrogen is closer to ~2000 K. Similar vibrational temperatures of the $N_2(C)$ molecule have been measured

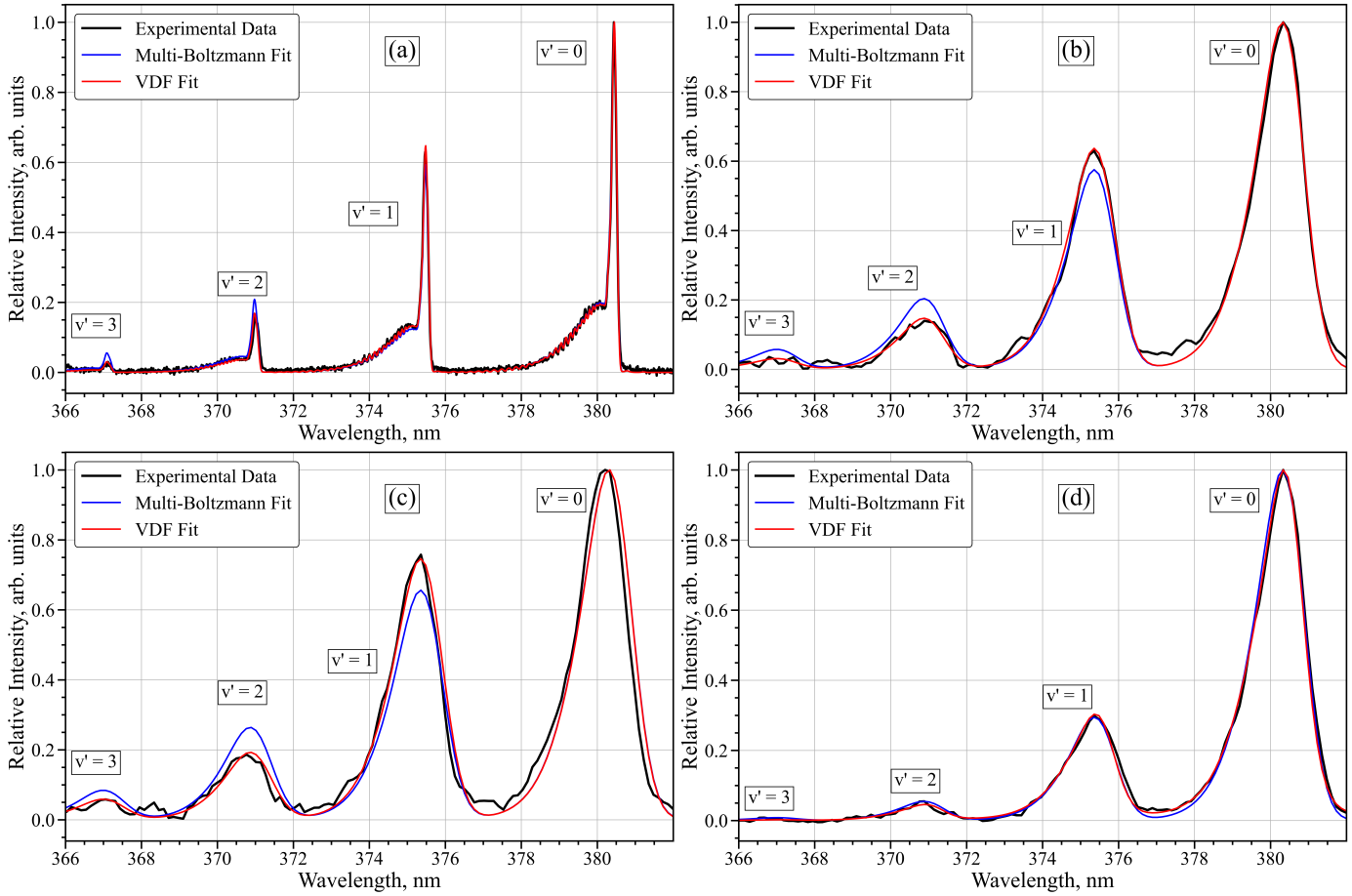

Figure 3: Comparison of experimental emission spectrum of $N_2(C \rightarrow B)$ taken with (a) Sandia experimental set-up with the ^{210}Po source compared to a multi-Boltzmann fit and a VDF fit in ambient air at T = 293 K, p = 83 kPa with best fit temperatures for the multi-Boltzmann fit being T_r = 360 K and T_v =3816 K. (b) PNNL experimental set-up with the ^{210}Po source compared to a multi-Boltzmann fit and a VDF fit in ambient air at T = 293 K, p = 101 kPa with the best fit temperatures for the multi-Boltzmann fit being T_v =3670 K. (c) PNNL experimental set-up with the ^{210}Po source compared to a multi-Boltzmann fit and a VDF fit in ambient air at T = 293 K, p = 15 kPa with the best fit temperatures for the multi-Boltzmann fit being T_v =4176 K. (d) PNNL experimental set-up with the ^{210}Po source compared to a multi-Boltzmann fit and a VDF fit in pure nitrogen at T = 293 K, p = 101 kPa with the best fit temperatures for the multi-Boltzmann fit being T_v = 1926 K.

Table 1: Inferred vibrational temperature of $N_2(C^3\Pi_u)$ for different band progressions from the Sandia and PNNL data set at local atmospheric pressure. All values are in Kelvin.

Source	Δv = 1	Δv = 0	Δv = -1	Δv =-2	Δv =-3	full spectrum
Sandia, air at p = 83 kPa	2622	3676	4204	3816	3605	3749
PNNL, air at p = 101 kPa	2899	3864	3793	3625	3410	4990
PNNL, air at p = 15 kPa	3284	5495	4538	4213	3659	4626
PNNL, N_2 at p = 101 kPa	2405	2966	1977	1926	1951	2432

in atmospheric air plasmas as well (25; 26; 27). The average fitted rotational temperature for $N_2(C^3\Pi_u)$ is T_{rot} = 352 ± 13 K for the Sandia data. The spectral resolution of the PNNL data was too low to fit for rotational temperature and was assumed to be 300 K. The vibrational temperature fit for $\Delta v = 1$ is lower for both spectrometers due to interference from the Gaydon-Herman bands identified in Ref. (10). The inferred vibrational temperature from the full spectrum fit, which includes only the band progressions given in Table 1, is much higher than the average vibrational temperature for the PNNL set-up in air. The higher inferred vibrational temperature is likely caused by interference of other electronic bands due to the increased spectral overlap from the lower resolution spectrometer.

Fitting the non-Boltzmann VDF model utilized the matrix behavior of Eq. 2 and was solved with SciPy's non-negative least squares solver for the VDF matrix. For fitting the VDF,

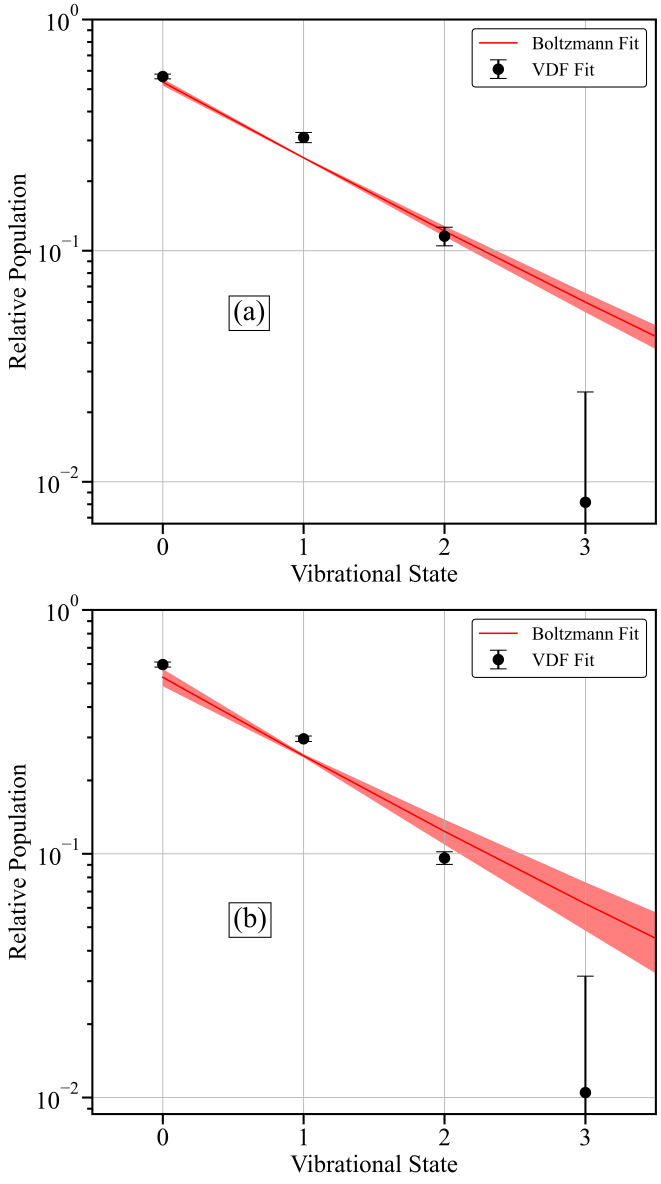

Figure 4: Comparison of the average fitted VDF and average inferred VDF from vibrational Boltzmann distribution for $N_2(C^3\Pi_u)$ in atmospheric air with (a) the Sandia source at T_{vib} = 3810 K and (b) in the PNNL source at T_{vib} = 3656 K.

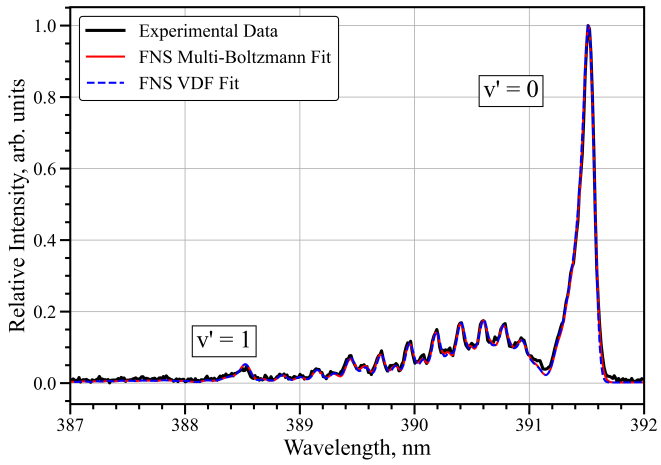

Figure 5: Comparison of experimental emission spectrum of $N_2^+(B)$ taken with Sandia experimental set-up with the ^{210}Po source compared to a multi-Boltzmann fit and a VDF fit. The best fit temperatures for the multi-Boltzmann fit give T_r = 361 K and T_v =1550 K.

the $\Delta\nu = 1$ band progression was ignored due to the lack of information for $v' = 0$ of the $C^3\Pi_u$ state. Additionally, for several band progressions the $v' = 3$ state had to be set to zero due to spectral inferences from other electronic systems or lack of emission signature due to weak Franck-Condon factors (23). For the $\Delta\nu = 0$, the Gaydon-Herman c_4' (0-4) overlaps the $v' = 3$ while the $\Delta\nu = -3$ overlaps with the (0-0) band for the first negative system at $v' = 3$. VDF values inferred from the Sandia and PNNL source are given in Table 2 for measurements in air and in nitrogen.

A comparison of the multi-Boltzmann and non-Boltzmann vibrational fitting approaches to the experimental data is shown in Fig. 3 for the $\Delta\nu = -2$ band progression near 380 nm for both the Sandia ^{210}Po source and the PNNL ^{210}Po source. The upper vibrational state of the $C^3\Pi_u$ state of N_2 is labeled next to the corresponding vibrational peaks in Fig. 3. Additional information on vibrational peak positions can be found in Ref. (23). This region was chosen due to the lack of interference from other electronic bands, such as the N_2^+ FNS, and because of the favorable Franck-Condon factors allowing for emission measurements up to $v = 3$ in the $C^3\Pi_u$ state. Comparison of ambient air at atmospheric conditions for Sandia and PNNL are shown in Fig. 3 (a) and (b), respectively. When pressure was decreased, as shown in Fig. 3(c), the vibrational temperature of $N_2(C^3\Pi_u)$ was seen to increase. Measurements in air done at 101, 79, 54, 37, and 15 kPa showed that a decrease in pressure leads to a linear increase in fitted vibrational temperature of the $N_2(C^3\Pi_u)$ state. For all the air cases analyzed, disagreement between the multi-Boltzmann spectral modeling and the experimental data was seen at the higher vibrational states of $N_2(C^3\Pi_u)$. Fit of emission spectra in pure nitrogen showed a dramatic decrease in the vibrational excitation of $N_2(C^3\Pi_u)$ as shown in Fig. 3(d). In contrast to the measurements performed in air, the vibrational distribution of $N_2(C^3\Pi_u)$ measured in pure nitrogen is essentially Boltzmann.

Table 1 and Table 2 give the fitted T_{vib} and the inferred VDF

Table 2: Inferred VDFs for different band progressions from designated Sandia and PNNL ^{210}Po sources.

v	Δv = 0	Δv =-1	Δv = -2	Δv =-3	full spectrum
0	0.56[a]	0.58	0.57	0.55	0.55
	0.60[b]	0.62	0.58	0.60	0.52
	0.44[c]	0.55	0.54	0.55	0.49
	0.70[d]	0.79	0.78	0.78	0.70
1	0.31	0.30	0.30	0.33	0.29
	0.30	0.29	0.29	0.30	0.35
	0.35	0.31	0.31	0.31	0.29
	0.30	0.19	0.18	0.18	0.22
2	0.13	0.11	0.10	0.12	0.10
	0.10	0.09	0.09	0.10	0.13
	0.12	0.15	0.10	0.14	0.11
	0.00	0.02	0.04	0.04	0.06
3	0[e]	0[e]	0.03	0[e]	0.06
	0[e]	0[e]	0.04	0[e]	0.08
	0.09	0[e]	0.05	0[e]	0.11
	0[e]	0[e]	0[e]	0[e]	0.02

[a] Sandia ^{210}Po source in air at 83 kPa
[b] PNNL ^{210}Po source in air at 101 kPa
[c] PNNL ^{210}Po source in air at 15 kPa
[d] PNNL ^{210}Po source in nitrogen
[e] Set equal to zero.

of $N_2(C^3\Pi_u)$ for the four cases shown in Fig. 3. A comparison of the average vibrational Boltzmann distribution from the multi-Boltzmann fitting for T_{vib} and the inferred VDF from the non-Boltzmann fitting for atmospheric pressure air is shown in Fig. 4. For the averages, the $\Delta v = 1$ value for Sandia and PNNL and the full spectrum fit for the PNNL were excluded from the analysis due to the spectral interferences discussed above. It is clear from the spectral fits shown in Fig. 3 and comparison of the inferred relative vibrational populations in Fig. 4 that the vibrational distribution measured from radioluminescence for the SPS is distinctly non-Boltzmann and is driven by the kinetics of the system.

The $N_2^+(B^2\Sigma_u^+ \rightarrow X^2\Sigma_g^+)$ FNS $\Delta v = 0$ spectrum near 391 nm from the Sandia experimental set-up was fit with the multi-Boltzmann and VDF approaches as shown in Fig. 5. The upper vibrational of the $B^2\Sigma_u^+$ of N_2^+ is labeled next to the corresponding vibrational peaks in Fig. 5. Additional information on the vibrational peak positions can be found in Ref. (24). Both fits included the contribution from $N_2(C^3\Pi_u, v = 3)$ from the $\Delta v = -3$ band at 389 nm. The multi-Boltzmann fitted temperatures of $N_2^+(B^2\Sigma_u^+)$ are T_{rot} = 361 and T_{vib} = 1550 K. The VDF fit returned relative vibrational populations of 0.90 and 0.10 for v = 0 and v = 1, respectively. The $N_2^+(B^2\Sigma_u^+)$ exhibits considerably less vibrational excitation than $N_2(C^3\Pi_u)$ at the same conditions and the vibrational distribution is nearly Boltzmann. The fitted rotational temperatures for $N_2(C^3\Pi)$ and $N_2^+(B^2\Sigma_u^+)$ both agree within uncertainties.

4. Kinetic Modeling

To help understand the radioluminescence response of ^{210}Po in air and nitrogen, a simple zero-dimensional kinetic model was developed to model the $N_2(C^3\Pi_u)$ VDF and the population ratio of $N_2(C^3\Pi_u)$ to $N_2^+(B^2\Sigma_u^+)$. The kinetic mechanism models the time-resolved populations of $N_2(X^1\Sigma_g^+)$, $N_2(C^3\Pi_u, v)$, $N_2^+(X^2\Sigma_g^+)$, $N_2^+(B^2\Sigma_u^+)$, N_4^+, O_2^+, and e^-. Inputs for the modeling are the initial pressure, temperature and mole fractions which is either pure N_2 or 20% O_2 and 80% N_2. The kinetic model had time steps of 3 ns for a total run time of 30 μs to ensure that all the species had reached steady-state. The full kinetic mechanism for modeling the radioluminescence is given in Table 3 which includes ionization, collisional de-excitation, electron impact excitation, spontaneous emission, vibrational-vibrational exchange, and recombination. Importantly, all the reactions that form and quench the $N_2(C^3\Pi)$ state must be vibrationally resolved for comparison with experimental data. The entire vibrational manifold of $N_2(C^3\Pi_u)$, v = 0–4, is modeled though $v = 4$ was not observed in any of the experimental data and cannot be validated with the kinetic mechanism. In addition, certain quenching rates for $N_2(C^3\Pi_u, v = 4)$ are not available in literature so they were assumed to be equal to v = 3.

The kinetic model assumes a steady-state background plasma with a Maxwellian electron energy distribution function (EEDF), driving impact excitations from ground state N_2 to the ionized N_2^+ and $N_2(C^3\Pi_u, v)$. The electron ionization cross-sections for N_2 to N_2^+ are divided into the $X^2\Sigma_g^+$ and $B^2\Sigma_u^+$ electronics states. The cross-sections for the ionization were obtained from (28; 29). Vibrationally-resolved electron excitation cross-sections for $N_2(C^3\Pi_u)$ were obtained from Malone et al. (30) for energies from 0–100 eV. The electron excitation cross-sections from 30 eV up to 600 eV shows a dependence on electron energy as a function of $E^{-2.3}$ (31). To avoid uncertain extrapolation of cross-sections above 100 eV from Ref. (30), the total electron excitation cross-section for $N_2(C^3\Pi_u)$ from 0–1000 eV is taken from Ref. (32). To obtain vibrationally-resolved electron excitation cross-sections, the total cross-section from Ref. (32) was multiplied by 0.48, 0.28, 0.08, 0.02, 0.005 for v = 0, 1, 2, 3, 4 to match the cross-sections from Ref. (30) for 0–100 eV.

A number of atoms and molecular states from Table 3 which would normally be considered are neglected in the kinetic modeling such as: $N_2(B^3\Pi_g)$, $N_2(A^3\Sigma_u^+)$, $N_2(a'^1\Sigma_u)$, atomic nitrogen, and atomic oxygen species. Reactions, such as R7, which would normally produce other electronic states, like $N_2(B^3\Pi_g)$, are modeled as being immediately quenched to the ground state, $N_2(X)$. Important reactions such as the energy pooling process of $N_2(A^3\Sigma_u^+)$ (40) which replenishes the $N_2(C^3\Pi_u)$ state are not included due to both the presence of ambient quantities of O_2 and low number densities of $N_2(A^3\Sigma_u^+)$ formed in these environments.

Initial kinetic modeling of the radioluminescence was unable to match the experimental VDF of $N_2(C^3\Pi_u)$ in air. Thus, an additional mechanism of $N_2(C^3\Pi_u, v)$ formation was added via the dissociative recombination of N_4^+ with electrons. First ob-

Table 3: The kinetic mechanisms and rates used in the coupled rate equation model of the ^{210}Po radioluminescence.

Reaction	Process	Rate coefficient	Reference
R1	$N_2(X^1\Sigma_g^+) + e^- \rightarrow N_2(C^3\Pi, v) + e^-$	f(eV)[a]	(30; 32)
R2	$N_2(X^1\Sigma_g^+) + e^- \rightarrow N_2^+(X^2\Sigma_g^+) + e^- + e^-$	f(eV)[a]	(28; 29)
R3	$N_2(X^1\Sigma_g^+) + e^- \rightarrow N_2^+(B^2\Sigma_u^+) + e^- + e^-$	f(eV)[a]	(28; 29)
R4	$N_2(C^3\Pi, v) + N_2(X^1\Sigma_g^+) \rightarrow N_2(X^1\Sigma_g^+) + N_2(X^1\Sigma_g^+)$	[1.3, 2.9, 4.6, 4.3, 4.3[b]][c]$\times 10^{-11}$	(33)
R5	$N_2(C^3\Pi, v) + N_2(X^1\Sigma_g^+, w) \rightarrow N_2(C^3\Pi, v') + N_2(X^1\Sigma_g^+, w')$	f(v)[d]	(34)
R6	$N_2(C^3\Pi, v) + O_2 \rightarrow N_2(X^1\Sigma_g^+) + O_2$	[3.0, 3.1, 3.7, 4.3, 4.3[b]][c]$\times 10^{-10}$	(33)
R7	$N_2(C^3\Pi, v) \rightarrow N_2(B^3\Pi_g) + h\nu$	[2.7, 2.7, 2.6, 2.6, 2.5][c]$\times 10^{7}$	(35)
R8	$N_2^+(X^2\Sigma_g^+) + N_2(X^1\Sigma_g^+) + N_2(X^1\Sigma_g^+) \rightarrow N_4^+ + N_2(X^1\Sigma_g^+)$	$6.8\times 10^{-29}(\frac{300}{T})^{1.64}$	(36)
R9	$N_2^+(B^2\Sigma_u^+) \rightarrow N_2^+(X^2\Sigma_g^+) + h\nu$	1.7×10^{7}	(37)
R10	$N_2^+(B^2\Sigma_u^+) + O_2 \rightarrow N_2^+(X^2\Sigma_g^+) + O_2$	6.8×10^{-10}	(37)
R11	$N_2^+(B^2\Sigma_u^+) + N_2(X^1\Sigma_g^+) \rightarrow N_2^+(X^2\Sigma_g^+) + N_2(X^1\Sigma_g^+)$	4.6×10^{-10}	(37)
R12	$N_4^+ + e^- \rightarrow N_2(M^e) + N_2(X^1\Sigma_g^+)$	$2.3\times 10^{-6}(\frac{300}{T_{electron}})^{0.5}(\frac{1}{2+\frac{180}{T}})$	(38)
R13	$N_4^+ + e^- \rightarrow N_2(C^3\Pi, v) + N_2(X^1\Sigma_g^+)$	A[f]$\times 2.3\times 10^{-6}(\frac{300}{T_{electron}})^{0.5}(\frac{\frac{180}{T}}{2+\frac{180}{T}})$	(38)
R14	$N_2^+(X^2\Sigma_g^+) + e^- \rightarrow N + N$	$2.8\times 10^{-7}(\frac{300}{T_e})^{0.5}$	(39)
R15	$N_2^+(X^2\Sigma_g^+) + O_2 \rightarrow N_2(X^1\Sigma_g^+) + O_2^+$	$6\times 10^{-22}(\frac{300}{T})^{0.5}$	(39)
R16	$N_4^+ + O_2 \rightarrow O_2^+ + N_2(X^1\Sigma_g^+) + N_2(X^1\Sigma_g^+)$	2.5×10^{-10}	(39)
R17	$N_4^+ + N_2(X^1\Sigma_g^+) \rightarrow N_2^+ + N_2(X^1\Sigma_g^+) + N_2(X^1\Sigma_g^+)$	$2.1\times 10^{-16}\ \exp(\frac{T}{121})$	(38)
R18	$O_2^+ + e^- \rightarrow O + O$	$2\times 10^{-7}(\frac{300}{T_e})$	(39)

[a] Rate is a function of electron temperature in eV.
[b] No rate for v =4. Rate assumed to be equal to v = 3.
[c] These rates are for $N_2(C^3\Pi_u)$ vibrational states for v = 0, 1, 2, 3, 4.
[d] Matrix of kinetic rates for each vibrational state of $N_2(C^3\Pi_u)$ going from $v \rightarrow v'$.
[e] M stands for different electronic states, i.e. M = $A^3\Sigma$ or $B^3\Pi$.
[f] Vibrational branching ratio givin in Table 4.

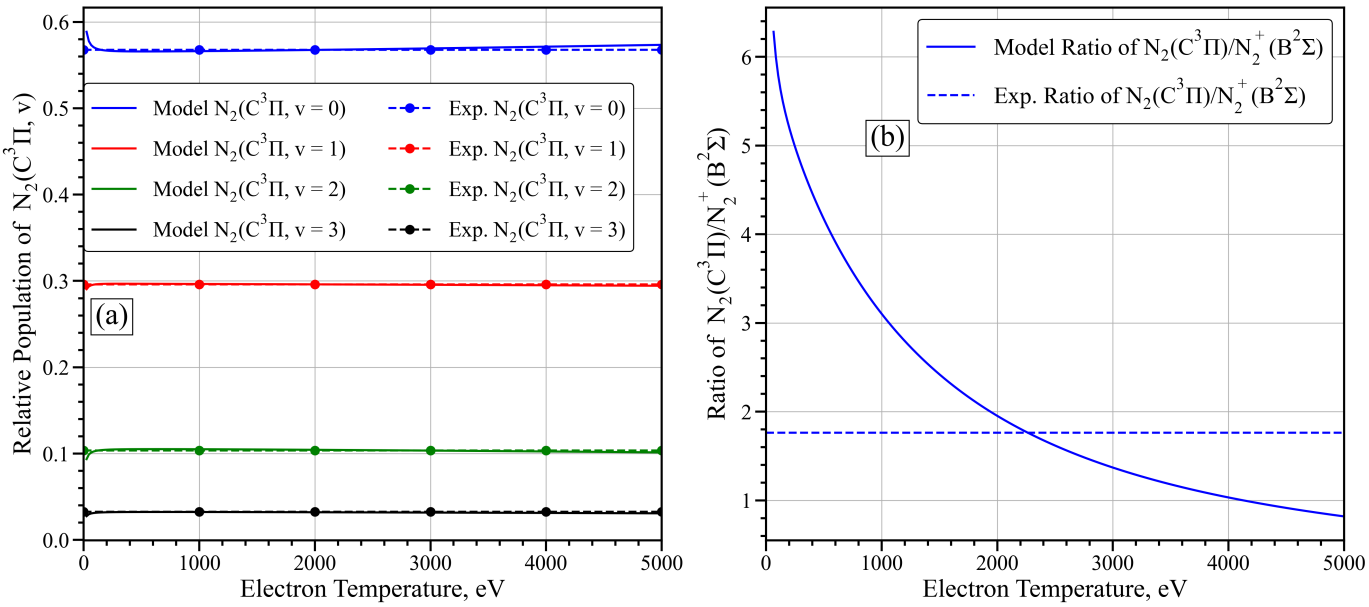

Figure 6: (a) Kinetic mechanism response of the VDF of $N_2(C^3\Pi_u)$ to range of electron temperature from 0 - 5000 eV with comparison to the fitted VDF from the Sandia experiment. (b) Change in the population ratio of $N_2(C^3\Pi_u)$ to $N_2^+(B^2\Sigma_u^+)$ from the kinetic mechanism with electron temperatures from 0 - 5000 eV with the comparison to the experimental ratio from Sandia experiment. The inferred experimental values were taken at only one condition and are overlaid with the model predictions with respect to electron temperature for comparison.

served by Sauer and Mulac (41), the dissociative recombination of N_4^+ was found to produce SPS emission. A number of studies have examined the kinetic rates of dissociative recombination of N_4^+ (42; 43; 44; 45; 36; 46). While there have been numerous studies on N_4^+ recombination, there have been no reports on the vibrational branching ratios into the $N_2(C^3\Pi)$ state (47). Thus, the kinetic model was used to fit the vibrational branching ratio of reaction R13 into $N_2(C^3\Pi_u, v)$ to match the experimental data. To fit the vibrational branching ratio of the dissociative recombination of N_4^+, the VDF of $N_2(C^3\Pi_u)$ inferred from Sandia's data and the ratio of population of $N_2(C^3\Pi_u)$ to $N_2^+(B^2\Sigma_u^+)$ were used as the objective function to minimize against with the vibrational branching ratio and the electron temperature, i.e electron kinetic energy, used as the fitting parameters. The population ratio of $N_2(C^3\Pi_u)$ to $N_2^+(B^2\Sigma_u^+)$ was determined with the SPEARS spectral modeling code by fitting the relative intensities of the Δv = -2 second positive system at 380 nm to the Δv = 0 of the first negative system at 391 nm. The determined population ratio was 1.762. Using a Nelder-Mead optimizer, the branching ratio for dissociative recombination of N_4^+ was determined and is given in Table 4. The model prediction response of the $N_2(C^3\Pi_u)$ VDF and the population ratio of $N_2(C^3\Pi_u)$ to $N_2^+(B^2\Sigma_u^+)$ was determined for a range of electron temperatures from 20–5000 eV as shown in Fig. 6 (a) and (b), respectively, for p = 83 kPa and T = 363 K in air. The inferred experimental values are overlaid on top of the model predictions in Fig. 6 to help assign a best fit electron temperature where the model predictions and the experimental data intersect. For Fig. 6(a), the $N_2(C)$ VDF model predictions show very little response to the electron temperature. The vibrational branching ratios for dissociative recombination of N_4^+ are thus not unique with regards to the electron temperature. Fig. 6(b) shows that the model prediction of the ratio of $N_2(C^3\Pi_u)$ to $N_2^+(B^2\Sigma_u^+)$ has sensitivity to the electron temperature and a best fit agreement at an electron temperature of 2275 eV.

Table 4: Vibrational branching for dissociative recombination of N_4^+ into $N_2(C^3\Pi_u, v)$.

v = 0	v = 1	v = 2	v = 3
0.448	0.339	0.159	0.054

A comparison of four different experimentally inferred VDFs from the $\Delta v = -2$ of the N_2 second positive to the kinetic modeling is shown in Fig. 7. Fig. 7(a) is the experimental VDF used to fit the vibrational branching ratio for dissociative recombination of N_4^+. The pressure dependence on the VDF is shown in Fig. 7(b) for the pressures of 15 and 101 kPa. , pressure only has a slight effect on the resulting $N_2(C)$ VDF. The kinetic model also agrees that a factor of 6.7x change in pressure has little effect on the predicted $N_2(C)$ VDF. Finally, the comparison of experimental $N_2(C^3\Pi_u)$ VDF to the kinetic model in pure nitrogen is shown in Fig. 7(c). The kinetic model reproduces the $N_2(C^3\Pi_u)$ VDF in N_2 with an overall good amount of agreement. The drastic change of $N_2(C)$ VDF in a pure nitrogen environment, as seen in Fig. 7(c), is primarily controlled by the quenching of oxygen via reaction R6. This was confirmed with the kinetic model. Overall, the kinetic modeling has good relative predictive capability but still needs validation with absolute emission measurements.

High-resolution measurements between 365-394 nm provide the ideal wavelength range to measure the $N_2(C^3\Pi_u)$ VDF and

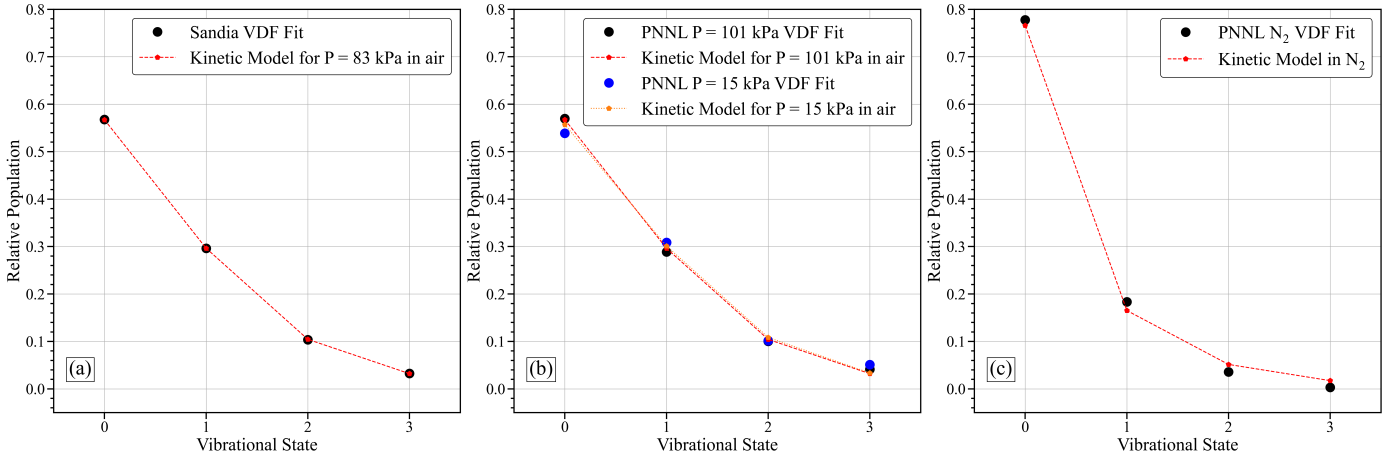

Figure 7: Comparison of $N_2(C^3\Pi_u)$ VDFs from the experimental emission spectra and calculated from the kinetic model for (a) Sandia's experimental set-up in air at p = 83 kPa, (b) PNNL's experimental set-up in air at p = 101 kPa and 15 kPa, and (c) PNNL's experimental set-up in pure N_2.

$N_2^+(B^2\Sigma_u^+)$ for relative populations of $N_2(C^3\Pi_u)$ and $N_2^+(B^2\Sigma_u^+)$. Fig. 8 shows the comparison of experimental data in air at 83 kPa and in pure nitrogen with respects to the the kinetic modeling predictions. The relative populations ratios of $N_2(C^3\Pi_u)$ compared to $N_2^+(B^2\Sigma_u^+)$ in air, for both Sandia and PNNL, is close to 1.7 while the population ratio in pure nitrogen is 7.8. While the kinetic model is able to match the experimental data in air, the modeling results for pure nitrogen over-predicts the population ratio of $N_2(C^3\Pi_u)$ to $N_2^+(B^2\Sigma_u^+)$ by a factor ~ 6.

The disagreement with the relative population of $N_2^+(B^2\Sigma_u^+)$, as shown in Fig. 8(b), may be due to missing kinetics in the mechanism. The mechanism assumes that alpha particle generate no fluorescence from $N_2^+(B^2\Sigma_u^+)$ when ionizing the air. Instead, it is assumed that the secondary electrons are the major contributors to the radioluminescence. This is commonly assumed when modeling radioluminescence from alpha particles (11; 48). Two additional kinetic processes not included in the kinetic mechanism could potentially be the cause of the discrepancy. The electron impact excitation with $N_2^+(B^2\Sigma_u^+)$ in reaction R19 could not be found in literature and is assumed to only have a small effect on the first negative emission.

$$N_2^+(X) + e^- \rightarrow N_2^+(B) + e^- \qquad \text{(R19)}$$

The second process involving vibrational - electronic energy exchange between high vibrational levels of $N_2(X)$ with $N_2^+(X)$

$$N_2(X, v \geq 12) + N_2^+(X) \rightarrow N_2(X, v-12) + N_2^+(B) \qquad \text{(R20)}$$

has been shown to be an important excitation pathway of $N_2^+(B^2\Sigma_u^+)$ in pure nitrogen environments (49). This unfortunately would require a dramatic increase in the number of molecular states being modeled and kinetic processes.

5. Summary and conclusions

In the present work, radioluminescence spectra were acquired from two ^{210}Po sources using high and low resolution spectrometers measuring from 250 - 400 nm in a range of different environments. Two different approaches for spectral analysis were employed to infer the vibrational distribution function of $N_2(C^3\Pi_u)$ molecule from the second positive system and $N_2^+(B^2\Sigma_u^+)$ molecule from the first negative system. The first approach analyzed the spectra using a multi-Boltzmann routine for fitting the rotational and vibrational temperatures separately.

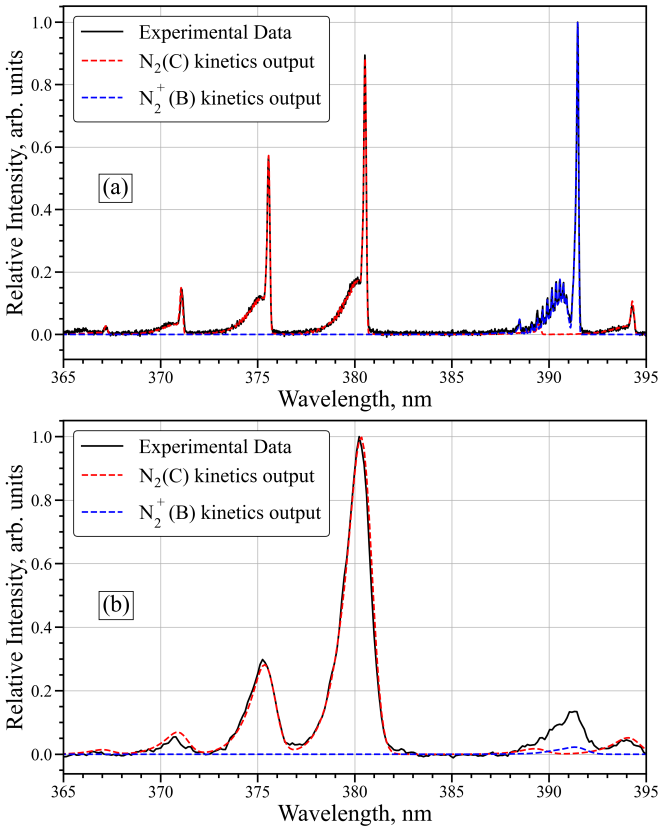

Figure 8: Kinetic modeling prediction for $N_2(C^3\Pi_u)$ VDF and relative populations of $N_2(C^3\Pi_u)$ and $N_2^+(B^2\Sigma_u^+)$ compared with experimental data from (a) Sandia in air at 83 kPa and (b) PNNL in nitrogen.

It was shown that the vibrational temperature of $N_2(C^3\Pi_u)$ increased with decreasing pressure in air and was substantially lower in nitrogen than air. The second approach directly fit for the VDF using a non-Boltzmann spectral model. The multi-Boltzmann approach used for fitting the vibrational temperature did not show good agreement with the data compared to the non-Boltzmann spectral fitting for the VDF. The fitted VDF from the non-Boltzmann spectral model was then used in development of a simple zero-dimensional kinetic model. The model is based on an assumed Maxwellian electron energy distribution function and a steady-state excitation and de-excitation processes. Initially, the kinetic model did not show good agreement with the experimental data. The inclusion of a vibrational branching ratio for the dissociative recombination of N_4^+ was able to produce excellent agreement with the experimental data in air and good agreement with the experimental data in nitrogen. The model was also able to match the relative populations of $N_2(C^3\Pi_u)$ and $N_2^+(B^2\Sigma_u^+)$ in air but over predicts the amount of $N_2(C^3\Pi_u)$ compared to $N_2^+(B^2\Sigma_u^+)$ in nitrogen. It is likely that the inclusion of $N_2(X)$ vibrational kinetics will improve the agreement in the population ratio seen between modeling and experiment in nitrogen. Overall, the model is the first step in developing a light-weight forward modeling capability for the prediction emission of radioluminescence from nitrogen containing environments. Additionally work is needed for validation of the model with absolute intensity calibrated emission spectra for accurate forward modeling.

Acknowledgements

The authors would like to thank Oskar Searfus for courteously providing the image of the ^{210}Po housing and false color images of the radioluminescence. The authors would also like to thank Zak Echo and Brian Bentz for reviewing this work.

This work was supported by the National Nuclear Security Administration (NNSA), Office of Defense Nuclear Nonproliferation Research and Development (NA-221) and the Defense Threat Reduction Agency (DTRA), Nuclear Technologies Detection Division.

This article has been authored by an employee of National Technology Engineering Solutions of Sandia, LLC under Contract No. DE-NA0003525 with the U.S. Department of Energy (DOE). The employee owns all right, title and interest in and to the article and is solely responsible for its contents. The United States Government retains and the publisher, by accepting the article for publication, acknowledges that the United States Government retains a non-exclusive, paid-up, irrevocable, world-wide license to publish or reproduce the published form of this article or allow others to do so, for United States Government purposes. The DOE will provide public access to these results of federally sponsored research in accordance with the DOE Public Access Plan https://www.energy.gov/downloads/doe-public-access-plan.

Pacific Northwest National Laboratory is a multi-program national laboratory operated by Battelle for the U.S. Department of Energy under Contract DE-AC05-76RL01830.

This paper describes objective technical results and analysis. Any subjective views or opinions that might be expressed in the paper do not necessarily represent the views of the U.S. Department of Energy or the United States Government.

References

[1] J. Brett, K. E. Koehler, M. Bischak, M. Famiano, J. Jenkins, L. Klankowski, P. Niraula, P. Pancella, R. Lakis, Spectral measurements of alpha-induced radioluminescence in various gases, Nuclear Instruments and Methods in Physics Research Section A: Accelerators, Spectrometers, Detectors and Associated Equipment 874 (2017) 88–93.

[2] J. Sand, S. Ihantola, K. Peräjärvi, H. Toivonen, J. Toivonen, Radioluminescence yield of alpha particles in air, New Journal of Physics 16 (5) (2014) 053022.

[3] S. M. Baschenko, Remote optical detection of alpha particle sources, Journal of radiological protection 24 (1) (2004) 75.

[4] D. L. Chichester, S. M. Watson, Multispectral uv-visual imaging as a tool for locating and assessing ionizing radiation in air, IEEE Transactions on Nuclear Science 58 (5) (2011) 2512–2518.

[5] F. Lamadie, F. Delmas, C. Mahe, P. Girones, C. Le Goaller, J. Costes, Remote alpha imaging in nuclear installations: New results and prospects, IEEE Transactions on Nuclear Science 52 (6) (2005) 3035–3039.

[6] E. Inrig, L. Erhardt, V. Koslowsky, B. Andrews, H. Ing, M. Dick, P. Forget, An air fluorescence imaging system for the detection of radiological contamination, in: Chemical, Biological, Radiological, Nuclear, and Explosives (CBRNE) Sensing XII, Vol. 8018, SPIE, 2011, pp. 119–124.

[7] F. S. Krasniqi, T. Kerst, M. Leino, J.-T. Eisheh, H. Toivonen, A. Röttger, J. Toivonen, Standoff uv-c imaging of alpha particle emitters, Nuclear Instruments and Methods in Physics Research Section A: Accelerators, Spectrometers, Detectors and Associated Equipment 987 (2021) 164821.

[8] C. O. Laux, T. Spence, C. Kruger, R. Zare, Optical diagnostics of atmospheric pressure air plasmas, Plasma Sources Science and Technology 12 (2) (2003) 125.

[9] S. Harilal, B. Brumfield, M. Phillips, An evaluation of equilibrium conditions and temperature-dependent speciation in a laser-produced air plasma, Physics of Plasmas 25 (8) (2018).

[10] G. Marshall, C. Murzyn, O. Searfus, S. S. Harilal, J. W. Inman, B. S. McDonald, R. Harrison, Informing solar blind radioluminescence imaging through a calibrated spectrum, Nuclear Instruments and Methods in Physics Research A (Under review).

[11] C. Thompson, E. Barritt, C. Shenton-Taylor, Predicting the air fluorescence yield of radioactive sources, Radiation Measurements 88 (2016) 48–54.

[12] J. Rosado, F. Blanco, F. Arqueros, On the absolute value of the air-fluorescence yield, Astroparticle Physics 55 (2014) 51–62. doi:https://doi.org/10.1016/j.astropartphys.2014.02.003.
URL https://www.sciencedirect.com/science/article/pii/S0927650514000152

[13] F. Arqueros, F. Blanco, J. Rosado, Improved model for the analysis of air fluorescence induced by electrons, Nuclear Instruments and Methods in Physics Research Section A: Accelerators, Spectrometers, Detectors and Associated Equipment 597 (1) (2008) 94–98, proceedings of the 5th Fluorescence Workshop. doi:https://doi.org/10.1016/j.nima.2008.08.043.
URL https://www.sciencedirect.com/science/article/pii/S0168900208012850

[14] F. Blanco, F. Arqueros, The role of secondary electrons in some experiments determining fluorescence emission from nitrogen c3u levels, Physics Letters A 345 (4) (2005) 355–361. doi:https://doi.org/10.1016/j.physleta.2005.07.059.
URL https://www.sciencedirect.com/science/article/pii/S0375960105011540

[15] I. Lalau, M.-R. Ioan, Simulation of radioluminescence induced by alpha particles in the air by the monte carlo method, RAD Conference Proc. 5 (2021) 37–41.

[16] M. Ribière, O. Eichwald, M. Yousfi, Microwave absorption and optical emission spectrometry analyses of ambient air plasmas induced by pulsed electron beams, Journal of Applied Physics 128 (9) (2020).

[17] N. Popov, Vibrational kinetics of electronically-excited molecules in nitrogen discharge plasma, Journal of Physics D: Applied Physics 46 (35) (2013) 355204.

[18] C. Richards, E. Jans, I. Gulko, K. Orr, I. V. Adamovich, N2 vibrational excitation in atmospheric pressure ns pulse and rf plasma jets, Plasma Sources Science and Technology 31 (3) (2022) 034001.

[19] O. Instruments, Typical spectra of oriel instruments spectral calibration lamps.
URL https://www.newport.com/medias/sys_master/images/images/h55/hfd/8797293281310/Typical-Spectra-of-Spectral-Calib-Lamps.pdf

[20] A. Lofthus, P. H. Krupenie, The spectrum of molecular nitrogen, Journal of physical and chemical reference Data 6 (1) (1977) 113–307.

[21] C. Murzyn, E. Jans, M. Clemenson, Spears: A database-invariant spectral modeling api, Journal of Quantitative Spectroscopy and Radiative Transfer 277 (2022) 107958.

[22] G. Dilecce, P. Ambrico, L. Martini, P. Tosi, On the determination of the vibrational temperature by optical emission spectroscopy, Plasma Sources Science and Technology 31 (7) (2022) 077001.

[23] E. Jans, Rovibronic molecular line list for the n2 (c3πu- b3πg) second positive system, Journal of Quantitative Spectroscopy and Radiative Transfer (2023) 108809.

[24] J. Luque, D. R. Crosley, Lifbase: Database and spectral simulation program (version 1.5), SRI international report MP 99 (009) (1999).

[25] T.-L. Zhao, Y. Xu, Y.-H. Song, X.-S. Li, J.-L. Liu, J.-B. Liu, A.-M. Zhu, Determination of vibrational and rotational temperatures in a gliding arc discharge by using overlapped molecular emission spectra, Journal of Physics D: Applied Physics 46 (34) (2013) 345201.

[26] D. Staack, B. Farouk, A. F. Gutsol, A. A. Fridman, Spectroscopic studies and rotational and vibrational temperature measurements of atmospheric pressure normal glow plasma discharges in air, Plasma sources science and technology 15 (4) (2006) 818.

[27] T. Shao, Y. Yu, C. Zhang, H. Jiang, P. Yan, Y. Zhou, Generation of atmospheric pressure plasma by repetitive nanosecond pulses in air using water electrodes, Plasma Science and Technology 13 (6) (2011) 735.

[28] Ist-lisbon database, www.lxcat.net, retrieved on 2023-11-16.

[29] L. Alves, The ist-lisbon database on lxcat, in: Journal of Physics: Conference Series, Vol. 565, IOP Publishing, 2014, p. 012007.

[30] C. Malone, P. Johnson, J. Young, X. Liu, B. Ajdari, M. Khakoo, I. Kanik, Integral cross sections for electron-impact excitation of the c 3πu, e 3σ+ g and a 1σ+ g states of n2, Journal of Physics B: Atomic, Molecular and Optical Physics 42 (22) (2009) 225202.

[31] J. T. Fons, R. S. Schappe, C. C. Lin, Electron-impact excitation of the second positive band system (c 3 π u→ b 3 π g) and the c 3 π u electronic state of the nitrogen molecule, Physical Review A 53 (4) (1996) 2239.

[32] Biagi database, www.lxcat.net, retrieved on 2023-11-16.

[33] S. Pancheshnyi, S. Starikovskaia, A. Y. Starikovskii, Collisional deactivation of n2 (c 3πu, v= 0, 1, 2, 3) states by n2, o2, h2 and h2o molecules, Chemical Physics 262 (2-3) (2000) 349–357.

[34] G. Dilecce, P. Ambrico, S. De Benedictis, Oodr-lif direct measurement of n2 (c 3πu, v= 0–4) electronic quenching and vibrational relaxation rate coefficients by n2 collision, Chemical physics letters 431 (4-6) (2006) 241–246.

[35] H.-J. Werner, J. Kalcher, E.-A. Reinsch, Accurate ab initio calculations of radiative transition probabilities between the a 3σ+ u, b 3π g, w 3δ u, b 3σ- u, and c 3π u states of n2, The Journal of chemical physics 81 (5) (1984) 2420–2431.

[36] H. Böhringer, F. Arnold, Temperature dependence of three-body association reactions from 45 to 400 k. the reactions n+ 2+ 2n2→ n+ 4+ n2 and o+ 2+ 2o2→ o+ 4+ o2, The Journal of Chemical Physics 77 (11) (1982) 5534–5541.

[37] F. Valk, M. Aints, P. Paris, T. Plank, J. Maksimov, A. Tamm, Measurement of collisional quenching rate of nitrogen states n2 (c 3πu, v= 0) and, Journal of Physics D: Applied Physics 43 (38) (2010) 385202.

[38] J. Levaton, A. Klein, C. Binder, Combined application of optical emission spectroscopy and kinetic numerical modelling to determine the ions densities in a flowing n 2 post-discharge, Plasma Chemistry and Plasma Processing 38 (2018) 1259–1272.

[39] I. Kossyi, A. Y. Kostinsky, A. Matveyev, V. Silakov, Kinetic scheme of the non-equilibrium discharge in nitrogen-oxygen mixtures, Plasma Sources Science and Technology 1 (3) (1992) 207.

[40] E. Jans, S. Raskar, X. Yang, I. Adamovich, Kinetics of metastable n2 (a3σu+, v) molecules in high-pressure nonequilibrium plasmas, Plasma Sources Science and Technology 30 (2) (2021) 025003.

[41] M. C. Sauer Jr, W. A. Mulac, Studies of light emission in the pulse radiolysis of gases: Electron-ion recombination in nitrogen, The Journal of Chemical Physics 56 (10) (1972) 4995–5004.

[42] P. Warneck, Studies of ion—neutral reactions by a photoionization mass-spectrometer technique. i, The Journal of Chemical Physics 46 (2) (1967) 502–512.

[43] Y. Cao, R. Johnsen, Recombination of n+ 4 ions with electrons, The Journal of chemical physics 95 (10) (1991) 7356–7359.

[44] M. Whitaker, M. A. Biondi, R. Johnsen, Electron-temperature dependence of dissociative recombination of electrons with n 2+· n 2 dimer ions, Physical Review A 24 (2) (1981) 743.

[45] Y. Ikezoe, S. Matsuoka, H. Nakamura, Recombination of n+ 4 and n+ 3 with electrons in atmospheric pressure nitrogen, Chemical physics letters 177 (4-5) (1991) 366–370.

[46] K. Keister, C. Wagner, J. Putney, J. Hewitt, J. G. Eden, Determination of ar 2+ and n 4+ recombination coefficients by subpicosecond multiphoton ionization at 248 nm and microwave interferometry, Physical Review A 89 (1) (2014) 013401.

[47] S. Adams, C. DeJoseph, J. Williamson, Formation and electron-ion recombination of n4+ following photoionization in near-atmospheric pressure n2, The Journal of chemical physics 130 (14) (2009).

[48] Z. Wu, J. Cheng, M. Xu, B. Wang, Q. Wang, A. Yu, Y. Zhang, W. Wen, Y. Wu, The physical mechanism of alpha-particle-air interaction and analysis of long-range secondary particles yield, Radiation Physics and Chemistry 202 (2023) 110426.

[49] B. F. Gordiets, C. M. Ferreira, V. L. Guerra, J. M. Loureiro, J. Nahorny, D. Pagnon, M. Touzeau, M. Vialle, Kinetic model of a low-pressure n/sub 2/-o/sub 2/flowing glow discharge, IEEE Transactions on Plasma Science 23 (4) (1995) 750–768.